



Effect of A-scan rate and interscan interval on optical coherence angiography

TING-HAO CHEN,¹ YI-CHUN WU,¹ TING-YEN TSAI,¹ CHUAN-BOR CHUEH,¹ BO-HUEI HUANG,² YIN-PENG HUANG,³ MENG-TSAN TSAI,^{2,4}  YOSHIAKI YASUNO,⁵  AND HSIANG-CHIEH LEE^{1,6,7,*} 

¹Graduate Institute of Photonics and Optoelectronics, National Taiwan University, Taipei 10617, Taiwan

²Department of Electrical Engineering, Chang Gung University, Taoyuan 33302, Taiwan

³Graduate Institute of Networking and Multimedia, National Taiwan University, Taipei 10617, Taiwan

⁴Department of Neurosurgery, Chang Gung Memorial Hospital, Linkou, Taoyuan 33306, Taiwan

⁵Computational Optics Group, University of Tsukuba, Tennodai 1-1-1, Tsukuba, Ibaraki 305-8573, Japan

⁶Department of Electrical Engineering, National Taiwan University, Taipei 10617, Taiwan

⁷Molecular Imaging Center, National Taiwan University, Taipei 10617, Taiwan

*hclee2@ntu.edu.tw

Abstract: Optical coherence tomography angiography (OCTA) can provide rapid, volumetric, and noninvasive imaging of tissue microvasculature without the requirement of exogenous contrast agents. To investigate how A-scan rate and interscan time affected the contrast and dynamic range of OCTA, we developed a 1.06- μm swept-source OCT system enabling 100-kHz or 200-kHz OCT using two light sources. After system settings were carefully adjusted, almost the same detection sensitivity was achieved between the 100-kHz and 200-kHz modalities. OCTA of ear skin was performed on five mice. We used the variable interscan time analysis algorithm (VISTA) and the designated scanning protocol with OCTA images reconstructed through the correlation mapping method. With a relatively long interscan time (e.g., 12.5 ms vs. 6.25 ms for 200-kHz OCT), OCTA can identify more intricate microvascular networks. OCTA image sets with the same interscan time (e.g., 12.5 ms) were compared. OCTA images acquired with a 100-kHz A-scan rate showed finer microvasculature than did other imaging modalities. We performed quantitative analysis on the contrast from OCTA images reconstructed with different A-scan rates and interscan time intervals in terms of vessel area, total vessel length, and junction density.

© 2021 Optical Society of America under the terms of the [OSA Open Access Publishing Agreement](#)

1. Introduction

Optical coherence tomography (OCT) is a real-time and noninvasive optical imaging technique that involves using low-coherence interferometry to provide volumetric imaging of architectural tissue information [1]. OCT has feasibility as a high-resolution imaging modality in various clinical applications such as those related to cardiology, dermatology, ophthalmology, and gastroenterology diseases [2]. OCT angiography (OCTA) is a functional extension of this technique that allows volumetric imaging of the subsurface microvasculature without the requirement of exogenous contrast agents. OCTA can be used for diagnostic assessments and the evaluation of new treatments along with the ongoing development of high-speed OCT imaging technology. To provide microvascular information of biological tissue, scientists have measured changes in the phase [3–7], amplitude (or intensity) [8–12], or complex values [13–17] of OCT signals resulting from the dynamic scattering of red blood cells in functional vessels relative to the static scattering of surrounding tissues. This approach can provide depth-resolved microangiograms with a capillary-level resolution, delineating three-dimensional (3D) microvascular networks in biological tissue.

Recently, OCTA has been implemented in human and animal models. In clinical medicine, using either commercial or in-house-developed OCT imaging systems, studies have demonstrated the applicability of OCTA in ophthalmology and dermatology for providing new insight into the pathophysiology, including the diseases of human eyes and skin [18–23]. In particular, OCTA can be performed in combination with standard OCT examination of the human retina, eliminating the need for a separate procedure. Repetitive OCTA can be performed as well, unlike conventional fluorescence angiography with ICG. However, studies have demonstrated the applicability of OCTA in various animal studies, either focusing on skin imaging or brain microvascular imaging. For example, Tsai *et al.* demonstrated the use of OCTA as a monitoring tool in transdermal drug-delivery systems with a mouse ear skin model [24]. Li *et al.* also employed an electrically tunable lens in a 1.3- μm spectral-domain OCT (SD-OCT) system to perform multi-focal-plane cerebral blood flow and optical microangiography imaging in mouse cortexes [25].

It is challenging to provide quantitative blood flow information with OCTA, even though OCTA can provide better visualization of the finer vascular network than Doppler OCT can. Studies have demonstrated the results of attempting to provide relative blood flow information with the variable interscan time analysis (VISTA) algorithm [26]. In this method, the dynamic range of OCTA can be adjusted with different interscan times of the repeated B-scans acquired at the same location. For example, OCTA with longer interscan time is more sensitive in detecting microvasculature with a lower blood flow rate relative to OCTA, with a shorter interscan time. Subsequently, by taking advantage of the aforementioned VISTA algorithm, Ploner *et al.* [27] provided OCTA image encoding relative blood flow information by employing OCTA images computed with two interscan times. The VISTA algorithm has successfully enhanced the dynamic range of OCTA for imaging the retinal vasculature of human eyes.

However, in these OCTA studies using the VISTA algorithm, researchers did not examine whether the effect of OCTA could be altered as a function of the light source A-scan rate and the interscan time for OCTA image reconstruction. In this study, therefore, we used a self-developed 1- μm OCT system to investigate the changes of OCTA contrast with different A-scan rates (100 kHz and 200 kHz) and interscan times between the repetitive OCT images used to reconstruct OCTA images. This study focused on comparing the OCTA images acquired using different A-scan rates but with the same interscan time. To avoid introducing bias into the contrast analysis of the OCTA results acquired with different A-scan rates, we adjusted the reference arm power to achieve almost the same detection sensitivity between the 100-kHz and 200-kHz OCT imaging modalities. In addition, parameters including the vessel area, total vessel length, and junction density were computed from the OCTA images acquired from five mouse ear skin models based on AngioTool (version 0.6a, National Institute of Health) [28].

2. Method

2.1. Swept-source OCT imaging system

Figure 1 presents a schematic of the 1- μm swept-source OCT (SS-OCT) system used in this study. Two separate light sources with a central wavelength of 1060 nm and a sweep rate of 100 kHz (Axsun Technologies) and 200 kHz (Axsun Technologies) were used alternatively in the SS-OCT system to provide OCT imaging with different A-scan rates. Ninety percent of the laser output was connected to the OCT interferometer; the remaining 10% of power was connected to a fiber Bragg grating (O\|E Land Inc.) to provide a stable A-scan trigger signal. In the sample arm, the light was collimated with an achromatic lens (AC080-016-C, Thorlabs) and directed to a pair of galvanometer scanning mirrors (GVS102, Thorlabs) to provide beam scanning over the sample surface. A single achromatic lens (AC254-060, Thorlabs) with a focal length of 60 mm was used in the sample arm, providing a lateral resolution of approximately 13.5 μm (full-width at half-maximum, FWHM) based on knife-edge measurements. The same optical components

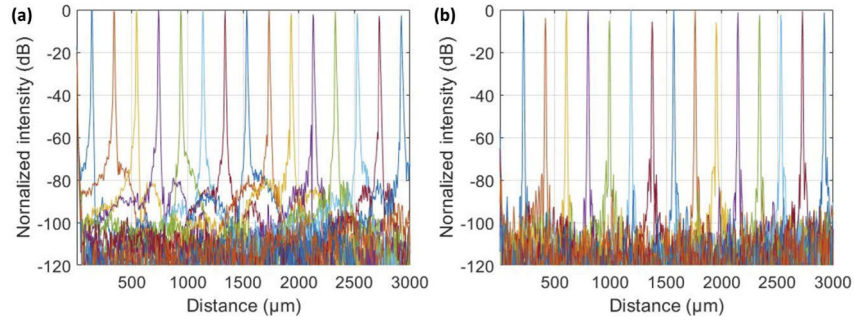


Fig. 2. Roll-off of the detection sensitivity for the SS-OCT system using the swept source with A-scan rates of (a) 100 kHz and (b) 200 kHz, respectively.

Table 1. Specifications of the 1.06- μm SS-OCT system employed in this study.

Swept source (Axsun Technologies)	100 kHz	200 kHz
Pixels per Ascan	1472 pixels	1312 pixels
Output power (light source)	15.4 mW	10.4 mW
Illumination power (sample)	1.7 mW	1.3 mW
Axial resolution (FWHM, in air)	10.4 μm	11.4 μm
Sensitivity (average)	94.0 dB	93.5 dB

2.2. OCTA image processing

Figure 3 displays the flowchart for the OCTA image processing with the correlation mapping algorithm used in this study. To perform OCTA, five repetitive B-scan frames were acquired at each location. Thus, one volumetric or 3D OCT raw data set contains $1000 \times 500 \times 5$ A-scans, where each B-scan frame consists of 1000 A-scans. After OCT images had been reconstructed from the raw data set, the OCT images were used to compute the OCTA images following the algorithm presented in Fig. 3. First, the correlation coefficients for each B-scan pixel were calculated based on Eq. (1) [11] to generate one correlation coefficient matrix, where I_A and I_B are the OCT signal intensity values in a linear scale format for the two adjacent frames selected from the five repeated frames.

$$I_{cm}(x, z) = \frac{\sum_{j=1}^M \sum_{k=1}^N \{ [I_A(x+k, z+j) - \overline{I_A(x, z)}] [I_B(x+k, z+j) - \overline{I_B(x, z)}] \}}{\sqrt{\sum_{j=1}^M \sum_{k=1}^N [I_A(x+k, z+j) - \overline{I_A(x, z)}]^2} \sqrt{\sum_{j=1}^M \sum_{k=1}^N [I_B(x+k, z+j) - \overline{I_B(x, z)}]^2}} \quad (1)$$

In Eq. (1), M and N represent the grid size or window size, and \bar{I} is the mean intensity for each grid. In our study, $M \times N$ was chosen to be 7×7 pixels corresponding to a matrix size of approximately $35 \mu\text{m} \times 27 \mu\text{m}$ and $37.8 \mu\text{m} \times 27 \mu\text{m}$ for the 100-kHz and 200-kHz OCT imaging, respectively, which achieved a reasonable balance between the imaging resolution and the OCTA image noise. The interval between the two frames used for the correlation coefficient calculation was not limited to 1 (i.e., adjacent frames), yielding a different interscan time for the OCTA contrast. For example, an interval of 1 frame (i.e., frame 1 \leftrightarrow frame 2, frame 2 \leftrightarrow frame 3, etc.) used to compute the OCTA images from the five repetitive B-scan frames corresponds to OCTA interscan times of 12.5 ms and 6.25 ms for the data sets acquired at rates of 100 kHz and 200 kHz, respectively. However, an interval of two frames allows an OCTA interscan time of 12.5 ms for 200-kHz OCT imaging.

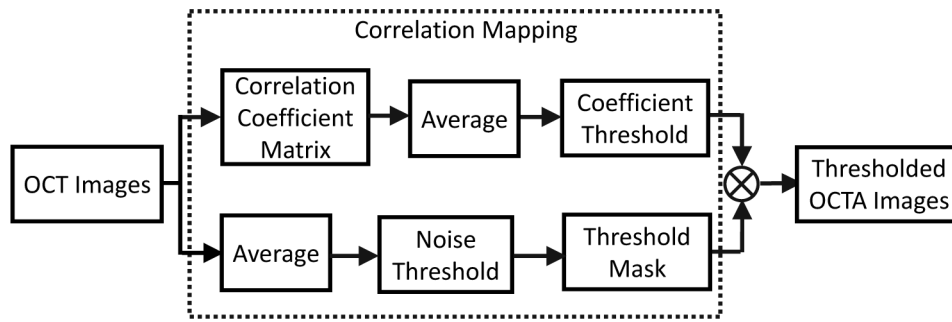


Fig. 3. Flowchart of the OCTA processing with the correlation mapping algorithm. By selecting the designated interval between the OCT images of the repetitive frames per location acquired using either a 100-kHz or a 200-kHz swept source, OCTA information with different interscan times can be computed afterward.

The calculated correlation coefficient matrices from the five repetitive frames based on the designated frame interval were averaged to improve the signal-to-noise ratio of the cross-sectional OCTA image. For example, for a frame interval of 1, the system has four correlation coefficient matrices to be averaged as one matrix. The averaged correlation coefficient matrix was thresholded based on the steps described in later passages. First, pixels with absolute correlation coefficients ranging from 0 to 0.6 were regarded to denote a potential location of blood flow. By contrast, any value outside this range was considered as the static background. Also, the noise floor of the averaged OCT images from the five repetitive frames was used to generate a mask. Finally, we applied this noise threshold mask to an averaged correlation coefficient matrix with consideration of the aforementioned threshold value to generate the final OCTA images.

Because five repetitive frames were acquired per location, the OCTA interscan time could be adjusted or varied by changing the frame interval used to compute the OCTA images, enabling the differentiation of microvasculature with different blood flow rates, similar to what can be achieved using the VISTA algorithm employed by Choi and Ploner *et al.* [26,27]. In this study, the duty cycle for scanning waveform along the fast axis for the galvanometer was 80%, yielding an OCTA interscan time of 12.5 ms for 200-kHz OCT imaging. All data processing, including the OCT and OCTA image reconstruction, was performed using MATLAB 2019b (MathWorks).

2.3. Animal imaging procedures

In this preliminary study, five small white ICR (Institute of Cancer Research) mice (BioLASCO, Taiwan) aged 5 weeks were used. The experimental procedure was approved (Protocol number: CGU105-062) by the Institutional Animal Care and Use Committee at Chang Gung University. Before the image session, each mouse was anesthetized with isoflurane, and the hair over the ear skin of mice was removed using hair removal cream. Mouse ears were temporarily fixed on a customized imaging holder using 3D printing technology during the OCT/OCTA session. For each mouse, 200-kHz OCT imaging was performed immediately after the 100-kHz OCT imaging by switching the 100-kHz swept source with the 200-kHz swept source after data saving had been completed. This approach ensures the imaging area is well registered between the 100-kHz and 200-kHz OCT imaging for each mouse. After both 100-kHz and 200 kHz OCT imaging sessions had been completed, the mouse was positioned in a separate chamber for recovery. A heat lamp was used to maintain mouse body temperature during the imaging session and the recovery stage. Subsequently, the same imaging protocol was performed for another mouse, until all five mice had been imaged.

2.4. Quantitative analysis of OCTA

AngioTool is a free, open-source software program that can be used to quantify blood vessel networks in microvascular images [28]. AngioTool provides some morphological and spatial parameters, including vessel area, the number of blood vessels, total vessel length, junction density, and the lacunarity. Studies have demonstrated the quantification of blood vessel networks with AngioTool in different animal studies such as in mouse brains, ratina, and human retina [29–33]. In this study, AngioTool allows the analysis of parameters including vessel area, total vessel length, and junction density for *en face* OCTA images, which are defined respectively as the area of the segmented vessels, the sum of Euclidean distances between the pixels of all the vessels, and the number of junctions per unit area. The parameters of the vessel diameter and vessel intensity in the AngioTool could be varied to dynamically update the vessel outline or detect the vessels at different spatial aspects. AngioTool can detect small blood vessels by applying smaller diameter parameter settings and eliminate the nonconnective pixels by removing the small particles and filling the holes. We set the vessel diameter parameters to 2 and 3, respectively, as the quantitative criteria for 100-kHz and 200-kHz OCT imaging of the ear skin from five mice.

3. Results

3.1. OCTA

Figure 4(a) presents a mouse ear skin photograph, where the ROI for OCT/OCTA is marked with a red box. The field of view (FOV) for the selected ROI is $3.85 \times 3.85 \text{ mm}^2$. Figures 4(b-d) illustrate the maximum projected *en face* OCTA image over the ROI reconstructed with the OCT images collected at a frame rate and A-scan rate of 80 Hz (interscan time of 12.5 ms) and 100 kHz [Fig. 4(b)], 160 Hz (interscan time of 6.25 ms) and 200 kHz [Fig. 4(c)], and 80 Hz (interscan time of 12.5 ms) and 200 kHz [Fig. 4(d)], respectively. A frame rate of 80 Hz corresponded to an OCTA interscan time of 12.5 ms. The number of A-scans per B-scan frame was kept at 1,000. More detailed microvasculature information can be observed in Fig. 4(b) [red arrows, Fig. 4(b)] relative to Fig. 4(d), even though Figs. 4(b, d) show the same OCTA interscan time but acquired with a different A-scan rate (100 kHz vs. 200 kHz). In addition, when a comparison was made between Figs. 4(c) and 4(d), it was revealed that the longer OCTA interscan time allowed the detection of microvasculature with a relatively slower blood flow [green arrows, Fig. 4(d)] [26,27,34] at the cost of being more vulnerable to the motion artifacts due to breathing. By computing the OCTA images with different OCTA interscan times based on the VISTA algorithm, as described previously [27], it provides relative blood flow information on the OCTA images, as depicted in Fig. 4(e), based on the OCTA images, as demonstrated in Figs. 4(c, d). The vessels with a larger diameter exhibited relatively faster blood flow than did those with smaller vessel diameters.

3.2. Comparison of OCTA contrast

Figure 5 presents a comparison of *en face* OCTA images of mouse ear skin (mouse D) reconstructed by using the OCT images acquired with either an SS-OCT of 100 kHz or 200 kHz and the OCTA algorithm with the designated interscan time. The *en face* OCTA images were cropped to $2.31 \times 2.31 \text{ mm}^2$ to avoid motion artifacts, such as those due to the breathing. These artifacts were represented as straight lines that usually occurred in the peripheral area of the original FOV. Thus, the OCTA images were cropped to avoid confounding the subsequent quantitative analysis of the OCTA images among different parameter settings. Figures 5(a–c) display raw *en face* OCTA images reconstructed with an OCTA interscan time and OCT A-scan rate of 12.5 ms and 100 kHz, 6.25 ms and 200 kHz, and 12.5 ms and 200 kHz, respectively. Figures 5(d–f) and Figs. 5(g–i) depict the analyzed results of Figs. 5(a–c) using AngioTool with the vessel diameters

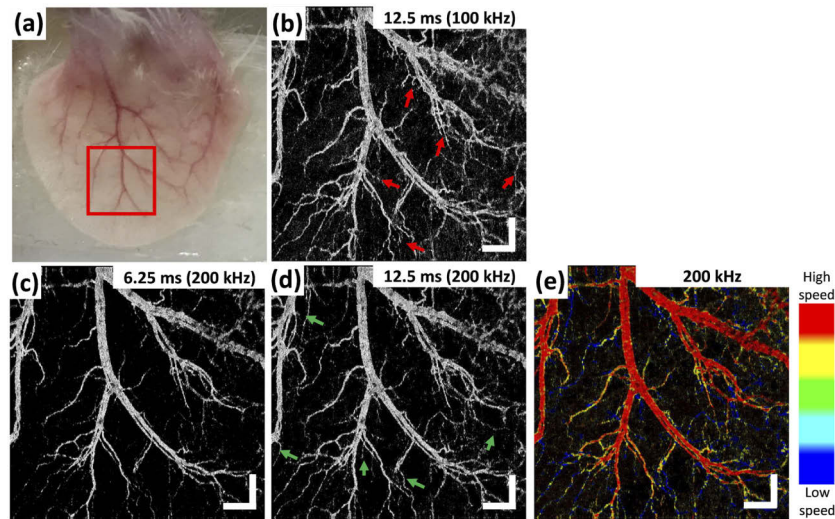


Fig. 4. *En face* OCTA images of the mouse ear skin (mouse B) based on the maximum projection of the OCTA signals. (a) The photograph of the mouse ear skin where the imaged site for OCT/OCTA are marked with a red box. (b-d) OCTA images over the marked region in (a), which were reconstructed with an OCTA interscan time and OCT A-scan rate of 12.5 ms and 100 kHz, 6.25 ms and 200 kHz, as well as 12.5 ms and 200 kHz, respectively. (e) Reconstructed OCTA images with relative blood flow information obtained using the VISTA algorithm (c, d). Scale bars: 0.5 mm.

of 2 and 3, respectively. In Figs. 5(d–i), the contour and skeleton of the vessel identified for the analysis are denoted in yellow and red, respectively. Increasing the parameter value of the vessel diameter revealed that only a microvasculature with a large vessel diameter would be identified and included for the vessel contour and skeleton labeling using *AngioTool*. Hence, more skeleton features marked in red in Figs. 5(d–f) could be observed relative to Figs. 5(g–i).

Table 2 summarizes the quantitative analysis for the *en face* OCTA images from five mice obtained using the *AngioTool*. As shown in Table 2, for the aforementioned three parameters, OCTA images with a longer interscan time had a larger value than those with a shorter interscan time. The values for the OCTA images computed with an OCTA interscan time of 6.25 ms and an A-scan rate of 200 kHz were always smaller than those images with an OCTA interscan time of 12.5 ms and A-scan rate of 200 kHz and an OCTA interscan time of 12.5 ms and A-scan rate of 100 kHz. Also, with the same OCTA interscan time, the values of the three parameters for the OCTA images acquired at the 100 kHz were larger than those acquired at 200 kHz. The last row of Table 2 shows the P values from the one-way Kruskal–Wallis analysis. In this test, the system had three groups with interscan times and A-scan rates of 12.5 ms and 100 kHz, 6.25 ms and 200 kHz, and 12.5 ms and 200 kHz, respectively, and each group had a sample of five mice. The P values were calculated using MATLAB 2019b (MathWorks) for individual parameters, including vessel area, total vessel length, and junction density. The final results indicate a rejection of the null hypothesis and an acceptance of the alternative hypothesis, with significance at the 5% significance level. The null hypothesis was that the medians of three groups were the same, and the alternative hypothesis was that at least one population median of one group was not equal to the population median of at least one other group.

Because three groups do not come from the overall same group under the 5% significance level, we again conducted a Wilcoxon signed-rank test to determine whether any two groups from the original three groups were statistically different. Table 3 shows that all P values associated

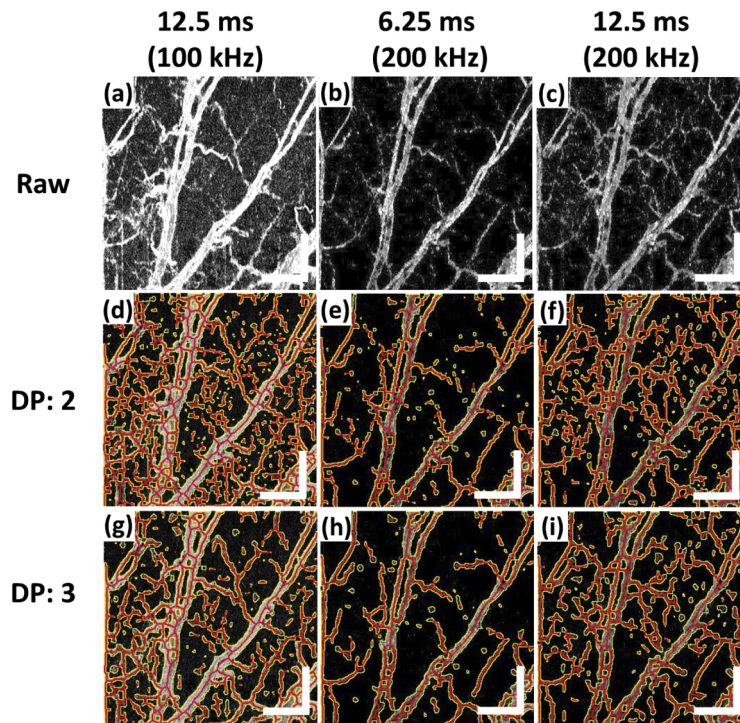


Fig. 5. Comparison of the *en face* OCTA images of the mouse ear skin (mouse D) between different interscan times in terms of the 100-kHz and 200-kHz swept sources. Figures 5(a–c) illustrate raw *en face* OCTA images with an image size of approximately $2.31 \times 2.31 \text{ mm}^2$ reconstructed with an OCTA interscan time and OCT A-scan rate of 12.5 ms and 100 kHz, 6.25 ms and 200 kHz, and 12.5 ms and 200 kHz, respectively. Figures 5(d–f) and (g–i) present the analyzed results of (a–c) obtained using AngioTool with vessel diameters of 2 and 3, respectively. After the AngioTool analysis algorithm was employed, the contour and skeleton of the microvasculature identified were marked in yellow and red, respectively. DP: diameter parameter Scale bars: 0.5 mm.

with any two groups are under the 5% significance level in terms of vessel parameters. The P values were calculated using MATLAB 2019b (MathWorks). Thus, the results of Table 3 indicate again that the test could reject the null hypothesis and accept the alternative hypothesis at the 5% significance level, where the null hypothesis is that the difference between the two groups arises from a distribution with a zero median. The alternative hypothesis is that the difference between the two groups originates from a distribution with a nonzero median.

Besides, the number of OCTA images averaged could affect its sensitivity to microvascular imaging. Therefore, we have computed the OCTA images for the 100-kHz OCT imaging with an interscan time of 12.5 ms by only using the first four of the five repetitive B-scan frames, i.e., only 3 correlation coefficient matrices were averaged to compute the OCTA image (Fig. 3). Note the same threshold value used to generate the noise mask for the OCTA images with 3 OCTA images averaged was used for the OCTA images with 4 OCTA images averaged for the 100-kHz OCT imaging. In order to quantitatively compare the changes of the OCTA images by reducing the number of OCTA images averaged for the 100-kHz OCT imaging, we also utilized AngioTool to assess the microvascular density exhibited in the OCTA images. Table 4 presents the comparison of the thresholded OCTA images for 100-kHz OCT imaging computed with 3 and 4 OCTA images averaged. As shown in Tables 4, a slight increase in most of the microvascular parameters

Table 2. Quantitative analysis results for the OCTA images of the ear skin of five mice using AngioTool.

Mouse ID	Interscan time (ms)	Vessel area (mm ²)		Total vessel length (mm)		Junction density (points/mm ²)	
		DP: 2	DP: 3	DP: 2	DP: 3	DP: 2	DP: 3
A	12.5 (100k)	3.710	2.921	80.833	60.870	125.850	64.796
	12.5 (200k)	3.021	2.550	68.890	52.034	90.168	47.433
	6.25 (200k)	2.531	2.187	61.304	43.485	74.119	29.716
B	12.5 (100k)	2.670	2.145	66.739	46.770	89.519	38.392
	12.5 (200k)	1.804	1.652	41.872	32.210	38.047	20.794
	6.25 (200k)	1.256	1.227	27.406	23.355	19.342	11.984
C	12.5 (100k)	2.778	2.407	67.042	49.670	88.183	43.161
	12.5 (200k)	2.470	2.242	57.155	45.247	67.180	36.560
	6.25 (200k)	1.869	1.869	42.260	36.283	40.838	24.408
D	12.5 (100k)	2.242	2.031	53.919	41.010	55.828	29.342
	12.5 (200k)	1.814	1.775	43.198	36.846	38.652	26.365
	6.25 (200k)	1.221	1.242	27.875	25.017	17.932	12.158
E	12.5 (100k)	1.352	1.365	30.594	27.698	20.557	15.279
	12.5 (200k)	1.021	1.065	23.564	22.075	13.241	11.603
	6.25 (200k)	0.678	0.724	16.239	14.999	9.237	6.433
P Value	12.5 (100k)_ 12.5 (200k)_ 6.25 (200k)	0.0295		0.0283		0.0384	

DP: Diameter Parameter.

Table 3. P values from the statistical analysis using the Wilcoxon signed-rank test between two groups with different frame rates or A-scan rates.

Interscan time (ms)	Vessel area	Total vessel length	Junction density
	P value	P value	P value
12.5 (100k)_12.5 (200k)	0.002	0.002	0.002
12.5 (100k)_6.25 (200k)	0.002	0.002	0.002
12.5 (200k)_6.25 (200k)	0.002	0.002	0.002

was observed in the thresholded OCTA images computed with 3 OCTA images averaged than that with the 4 OCTA images.

Table 4. Quantitative analysis results using AngioTool for the OCTA images of the ear skin of five mice with interscan time 12.5 ms and A-scan rate 100 kHz in terms of three and four OCTA frames averaged.

Mouse ID	No. of OCTA frames averaged	vessel area (mm ²)		total vessel length (mm)		junction density (points/mm ²)	
		DP: 2	DP: 3	DP: 2	DP: 3	DP: 2	DP: 3
A	3	3.737	2.947	80.578	62.797	121.885	71.161
	4	3.710	2.921	80.833	60.870	125.850	64.796
B	3	2.695	2.166	67.068	46.734	92.141	38.205
	4	2.670	2.145	66.739	46.770	89.519	38.392
C	3	2.854	2.443	67.862	50.256	87.517	43.794
	4	2.779	2.407	67.042	49.670	88.183	43.161
D	3	2.334	2.058	57.394	41.927	62.724	31.026
	4	2.242	2.031	53.919	41.010	55.828	29.342
E	3	1.395	1.401	32.061	28.477	22.950	17.161
	4	1.352	1.365	30.594	27.698	20.557	15.279

Table 5 shows the quantitative comparison of microvasculature in terms of vessel area, total vessel length, and junction density between the *en face* OCTA images acquired at A-scan rates of 100 kHz and 200 kHz but with the same OCTA interscan time (12.5 ms), as listed in Table 2. To perform an objective comparison of the three aforementioned microvasculature parameters, we introduced the metric η to perform quantitative assessments of any of the three microvascular parameters between the analyzed *en face* OCTA images acquired with different A-scan rates. The metric is defined in the following equation.

$$\eta = \frac{QA_{100 \text{ kHz}} - QA_{200 \text{ kHz}}}{(QA_{100 \text{ kHz}} + QA_{200 \text{ kHz}})/2} \quad (2)$$

In three microvascular parameters, the metric η is always larger than zero, suggesting that finer microvasculature can be detected in the *en face* OCTA images acquired at a lower A-scan rate. In addition, when we compared η values between the analyzed *en face* OCTA images with vessel diameters of 2 and 3, the η value was smaller for the later ones in terms of vessel area, total vessel length, and junction density. This suggests that for larger size blood vessels, using a 100-kHz light sources did not outperform the 200-kHz light source significantly.

Table 5. Quantitative comparison of microvasculatures between the *en face* OCTA images acquired at A-scan rates of 100 kHz and 200 kHz but with the same OCTA interscan time of the ear skin from five mice.

	Diameter parameter	A	B	C	D	E	Mean	Standard deviation
Vessel area (mm ²)	2	0.051	0.097	0.030	0.053	0.070	0.060	0.022
	3	0.034	0.065	0.018	0.034	0.062	0.043	0.018
Total vessel length (mm)	2	0.040	0.115	0.040	0.055	0.065	0.063	0.028
	3	0.039	0.092	0.024	0.027	0.057	0.048	0.025
Junction density (points/mm ²)	2	0.083	0.202	0.068	0.091	0.108	0.110	0.048
	3	0.078	0.149	0.042	0.027	0.069	0.073	0.042

Finally, as mentioned previously, the *en face* OCTA images were cropped to exclude regions with strong motion artifacts for the subsequent quantitative microvasculature analysis with *AngioTool*. The selection of the ROI of the *en face* OCTA images was based on a previously discussed rationale. Figure 6 shows an example of the *en face* OCTA image where motion artifacts could be observed at the lower-left part of the FOV. We performed the same quantitative analysis on the cropped *en face* OCTA images from three randomly selected ROIs, as marked by red, purple, and green boxes in Fig. 6. As summarized in Table 6, the metric η was always larger than zero for the three microvascular parameters over the three ROIs. Also, η was smaller for the analyzed *en face* OCTA image with a vessel diameter of 3 than that with a vessel diameter of 2.

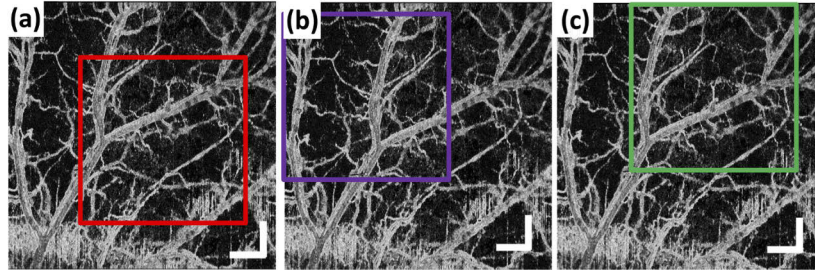


Fig. 6. Example *en face* OCTA image of the mouse ear skin (mouse C) where three ROIs were randomly selected as marked by (a) red, (b) purple, and (c) green boxes for the subsequent quantitative analysis of the microvasculature. Motion artifacts in images due to breathing can be observed at the lower-left corner of Figs. 6(a–c). Scale bar: 0.5 mm.

4. Discussion

Of various OCTA algorithms, the intensity signal-based OCTA image [35,36] could be used to image vasculature with slow blood flow and an increased dynamic range. This could be achieved using the VISTA algorithm [26,27,37] based on the BM mode scanning mechanism [5]. Another approach is to change the scanning mechanism using a bidirectional scanning pattern without sacrificing the total scan duration [34]. In related studies, the OCTA algorithm has been used to calculate the decorrelation value, which ranges from 0 to 1, where 0 and 1 respectively indicate the lowest and highest dissimilarity [12,38]. By contrast, our system with sweep sources of either 200 kHz or 100 kHz can also reveal vasculature variations between different scan intervals, and the dynamic range could also be increased using the BM mode through the correlation mapping algorithm. According to the OCTA algorithm used in this study, as depicted in Fig. 3, the correlation coefficient with threshold and absolute values thereof ranged from 0 to 0.6. Also, the meaning of the value in terms of dissimilarity was opposite to that in the decorrelation method [11].

According to some researchers [34,39], the decorrelation value of OCTA can be defined as 1 minus the normalized autocorrelation function of the light field, as presented in Eq. (3),

$$I_{de} = 1 - \exp\left(-\frac{|\tau|}{\tau_c}\right) \quad (3)$$

where τ_c is correlation time and τ is time difference corresponding to the frame interval or interscan time. In addition, the correlation coefficient of each pixel, as specified in Eq. (1), could be mapped into a normalized autocovariance function of the light field, as expressed in Eq. (4) [similar to Eq. (3)].

$$I_{cm} = \exp\left(-\frac{2\tau}{\tau_c}\right) \quad (4)$$

$$\tau_c \cdot (v_{flow} + v_{bulk} + v_{browian}) = \xi \quad (5)$$

Given that τ_c has a linear relationship with motion (as described in [34]), inclusive of flow rate v_{flow} , bulk motion v_{bulk} , and Brownian motion $v_{browian}$ [as formulated in Eq. (5)], where ξ is a constant, we can derive Eq. (6) by combining Eq. (3) and Eq. (5).

$$I_{cm} = \exp\left[-\frac{\tau \cdot (v_{flow} + v_{bulk} + v_{browian})}{\xi}\right] \quad (6)$$

Although the interscan time τ was different between 100 kHz and 200 kHz OCT imaging, a longer interscan time (12.5 ms) provides more detailed blood vessel information than does a

shorter interscan time (6.25 ms). This can be explained with reasoning similar to that in [34]. When interscan time τ increases, at the same blood flow rate, the correlation coefficient I_{cm} , as formalized in Eq. (6), decreases, making this value smaller than the threshold value. Equation (6) indicates that when interscan time increases (i.e., longer interscan time), a lower blood flow rate can be detected, thereby improving the slowest detectable flow. Similarly, Choi *et al.* [26] and Braaf *et al.* [40] also indicated a longer interscan time could improve the slowest detectable flow to facilitate the visualization of the capillary network in human eyes using decorrelation method OCTA and phase-resolved OCTA, respectively. Besides, with a shorter interscan time, the OCTA dynamic range between the slowest detectable flow and the fastest distinguishable flow could increase with the cost of compromising the slowest distinguishable flow [26]. Recently, Migacz *et al.* [41] also indicated the interscan time could play important role in contrast enhancement of OCTA images.

In general, the effect of interscan variation on the OCTA imaging will be most pronounced when the blood flow is not in the so-called saturation regime [26]. In particular, if the blood flow is flowing sufficiently fast, the OCTA signal will be, notwithstanding bulk motion or other higher order considerations, near to saturation regime and invariant to the interscan time. In this study, when comparing the OCTA images between the interscan time of 6.25 ms and 12.5 ms for the 200-kHz OCT imaging, the majority of the vessels appear to be at or near to the saturation regime (Fig. 4). Thus, an even shorter interscan time would likely allow greater increase in dynamic range.

On the other hand, the OCTA images from the 100-kHz OCT modality contained more detailed and clearer vasculatures than did the OCTA images from the 200-kHz OCT modality with the same B-scan interscan time τ (12.5 ms) and nearly the same sensitivity. Our results indicated that the correlation time τ_c or constant ξ of the 100-kHz OCT modality was less than that of the 200-kHz OCT modality, leading to an increased dynamic range, according to Eq. (4) or Eq. (6). Hence, the increased dynamic range also suggests that metric η listed in Tables 5 and 6 in terms of vessel area, total vessel length, and junction density for different vessel diameter parameters could all be positive values. Apart from the correlation time τ_c or constant ξ , the comparable or higher axial and lateral resolution of OCT images could benefit the visualization of capillary network [36]. However, the axial and lateral resolution were near the same for both 100-kHz and 200-kHz OCT system in our study. Besides, the number of OCTA images averaged to compute the final OCTA image per location was 3 and 4 for the 200-kHz and 100-kHz OCT imaging with an interscan time of 12.5 ms, respectively. As shown in Tables 4, an increase in most of the microvascular parameters was observed in the OCTA images computed with 3 OCTA images averaged than that with the 4 OCTA images averaged. It could be expected when the number of the OCTA images averaged decreases, the background noise could be increased due to the decreased signal-to-noise (SNR) ratio. Nevertheless, according to Tables 2 and 4, for either the number of the OCTA images averaged for 100-kHz OCT imaging, there exists a significant difference in the OCTA images computed between 100-kHz and 200-kHz OCT imaging with the 12.5 ms interscan time.

Some artifacts from bulk motion either caused by the respiration or the heart beating of mouse could not be easily removed without further image processing [42]. In the current study, although with the same OCTA interscan time, the OCTA images reconstructed from the 100-kHz OCT imaging showed more minute blood vessels of mouse ear skin than those with the 200-kHz OCT imaging. Because the peripheral areas of the mouse ear cannot easily and entirely be joined together with a sample holder, performing OCTA over the peripheral area of the original FOV made our images more vulnerable to influence from the aforementioned artifacts during 100-kHz OCT imaging than during 200-kHz OCT imaging. As illustrated in Fig. 6, motion artifacts are more prominent at the bottom part of the peripheral region, which is close to the mouse body. Thus, to perform an objective comparison of the microvascular parameters for

Table 6. Quantitative comparison of microvasculature between the *en face* OCTA images of mouse ear skin from three randomly selected ROIs shown in Fig. 6. Regions 1-3 correspond to ROIs marked by red, purple, and green boxes, respectively, in Fig. 6.

	Diameter parameter	Region 1	Region 2	Region 3	Mean	Standard deviation
Vessel area (mm ²)	2	0.030	0.017	0.030	0.026	0.006
	3	0.018	0.014	0.014	0.015	0.002
Total vessel length (mm)	2	0.040	0.040	0.046	0.042	0.003
	3	0.024	0.031	0.028	0.028	0.003
Junction density (points/mm ²)	2	0.068	0.069	0.091	0.076	0.011
	3	0.042	0.042	0.036	0.040	0.003

the OCTA modalities with different A-scan rates, cropped *en face* OCTA images were used for the subsequent analysis with AngioTool to avoid compromising or confounding the quantitative analysis.

Physiological functions of mice vary with time, leading to blood flow rate variations. Thus, the blood flow rate might be altered during measurement with 100-kHz and 200-kHz OCT imaging, which could be another error source for the quantified values in Tables 2 to 6. The swept source with a quickly tunable A-scan rate provided benefits and reduced errors due to a longer interval between the two aforementioned experiments. Moreover, as AngioTool was used to conduct the quantified analysis, we did not eliminate all nonconnective pixels (background noise or nonconnective finer capillary) by removing small particles and filling the holes in the original OCTA images to fairly and accurately compare the results of OCTA images of ear skin from five mice. This limitation could also affect the values of vessel parameters listed in Tables 2 to 6 and the distributions of skeletons (Figs. 5(d-i)) of mice ear skin.

If the sample arm power for 200-kHz OCTA under safety specifications could be enhanced, a higher dynamic range may be achieved for observing the same tiny capillaries from a 100-kHz swept source with the same interscan time. Currently, the sample arm power transferred to the sample presented in Table 1 for both swept sources is still below the American National Standards Institute (ANSI) limit of 14.49 mW and 24.38 mW for human skin at the center wavelength of 1060 nm and bandwidth of 100 nm [43]. Therefore, our 200-kHz system configuration has a considerable margin for increasing the sample arm power of future OCTA of human skin. Future approaches will have advantages of higher speed, lower bulk motion effects, and either higher ranges or almost the same dynamic ranges of OCTA images compared with the original 100-kHz system.

5. Conclusion

In this study, we developed an SS-OCT imaging modality enabling either 100-kHz or 200-kHz OCT imaging by using two separate light sources. In addition, using the VISTA algorithm and the correlation mapping method, the intricate microvascular network of the mouse ear skin could be identified using OCTA. OCTA processes with different interscan times were compared; either 100-kHz or 200-kHz OCT showed finer microvasculature at a longer interscan time (e.g., 12.5 ms vs. 6.25 ms), suggesting an enhanced dynamic range of OCTA with the VISTA algorithm. VISTA and OCTA produced results for the ears of five mice; the framework allows the identification of finer microvasculature from 100-kHz OCT imaging than from 200-kHz OCT imaging with the same interscan time and a similar OCT system sensitivity. With the AngioTool, the quantitative analysis results have confirmed the previous observation through analyzing the *en face* OCTA images with the parameters, including vessel area, total vessel length, and junction density. In conclusion, the results of this study should lead to future improvements in the dynamic range of OCTA detection.

Funding. Japan Society for the Promotion of Science (18H01893); Japan Science and Technology Agency (JPMJMI18G8); National Taiwan University (NTU-IOTP-108PNTUS05, NTU-IOTP-109PNTUS05); Ministry of Science and Technology, Taiwan (107-2636-E-002-003, 108-2636-E-002-009, 109-2636-E-002-028).

Acknowledgments. The authors acknowledge the support from the Young Scholar Fellowship Program of the Ministry of Science and Technology (MOST) of Taiwan, Republic of China (ROC), (MOST-107-2636-E-002-003, 108-2636-E-002-009, and 109-2636-E-002-028), National Taiwan University (NTU-IOTP-108PNTUS05 and NTU-IOTP-109PNTUS05), Japan Science and Technology Agency (JPMJMI18G8) and Japan Society for the Promotion of Science (18H01893). Facility support was provided by the Molecular Imaging Center (MIC) at National Taiwan University. This article was subsidized by the Ministry of Science and Technology and National Taiwan University (NTU), Taiwan.

Disclosures. The authors declare that there are no conflicts of interest related to this article.

References

1. D. Huang, E. A. Swanson, C. P. Lin, J. S. Schuman, W. G. Stinson, W. Chang, M. R. Hee, T. Flotte, K. Gregory, and C. A. Puliafito, "Optical coherence tomography," *Science* **254**(5035), 1178–1181 (1991).
2. E. A. Swanson and J. G. Fujimoto, "The ecosystem that powered the translation of OCT from fundamental research to clinical and commercial impact [Invited]," *Biomed. Opt. Express* **8**(3), 1638–1664 (2017).
3. R. A. Leitgeb, L. Schmetterer, W. Drexler, A. F. Fercher, R. J. Zawadzki, and T. Bajraszewski, "Real-time assessment of retinal blood flow with ultrafast acquisition by color Doppler Fourier domain optical coherence tomography," *Opt. Express* **11**(23), 3116–3121 (2003).
4. S. Makita, Y. Hong, M. Yamanari, T. Yatagai, and Y. Yasuno, "Optical coherence angiography," *Opt. Express* **14**(17), 7821–7840 (2006).
5. J. Fingler, D. Schwartz, C. H. Yang, and S. E. Fraser, "Mobility and transverse flow visualization using phase variance contrast with spectral domain optical coherence tomography," *Opt. Express* **15**(20), 12636–12653 (2007).
6. S. M. R. Motaghianezam, D. Koos, and S. E. Fraser, "Differential phase-contrast, swept-source optical coherence tomography at 1060 nm for in vivo human retinal and choroidal vasculature visualization," *J. Biomed. Opt.* **17**(2), 026011 (2012).
7. R. Poddar, D. Y. Kim, J. S. Werner, and R. J. Zawadzki, "In vivo imaging of human vasculature in the chorioretinal complex using phase-variance contrast method with phase-stabilized 1- μ m swept-source optical coherence tomography," *J. Biomed. Opt.* **19**(12), 1 (2014).
8. J. K. Barton and S. Stromski, "Flow measurement without phase information in optical coherence tomography images," *Opt. Express* **13**(14), 5234–5239 (2005).
9. A. Mariampillai, B. A. Standish, E. H. Moriyama, M. Khurana, N. R. Munce, M. K. K. Leung, J. Jiang, A. Cable, B. C. Wilson, I. A. Vitkin, and V. X. D. Yang, "Speckle variance detection of microvasculature using swept-source optical coherence tomography," *Opt. Lett.* **33**(13), 1530–1532 (2008).
10. J. Enfield, E. Jonathan, and M. Leahy, "In vivo imaging of the microcirculation of the volar forearm using correlation mapping optical coherence tomography (cmOCT)," *Biomed. Opt. Express* **2**(5), 1184–1193 (2011).
11. E. Jonathan, J. Enfield, and M. J. Leahy, "Correlation mapping method for generating microcirculation morphology from optical coherence tomography (OCT) intensity images," *J. Biophotonics* **4**(9), n/a (2010).
12. Y. L. Jia, O. Tan, J. Tokayer, B. Potsaid, Y. M. Wang, J. J. Liu, M. F. Kraus, H. Subhash, J. G. Fujimoto, J. Hornegger, and D. Huang, "Split-spectrum amplitude-decorrelation angiography with optical coherence tomography," *Opt. Express* **20**(4), 4710–4725 (2012).
13. R. K. Wang, S. L. Jacques, Z. Ma, S. Hurst, S. R. Hanson, and A. Gruber, "Three dimensional optical angiography," *Opt. Express* **15**(7), 4083–4097 (2007).
14. Y. K. Tao, A. M. Davis, and J. A. Izatt, "Single-pass volumetric bidirectional blood flow imaging spectral domain optical coherence tomography using a modified Hilbert transform," *Opt. Express* **16**(16), 12350–12361 (2008).
15. R. K. K. Wang, L. An, S. Saunders, and D. J. Wilson, "Optical microangiography provides depth-resolved images of directional ocular blood perfusion in posterior eye segment," *J. Biomed. Opt.* **15**(2), 020502 (2010).
16. W. J. Choi, R. Reif, S. Yousefi, and R. K. Wang, "Improved microcirculation imaging of human skin in vivo using optical microangiography with a correlation mapping mask," *J. Biomed. Opt.* **19**(3), 036010 (2014).
17. C. L. Chen, W. S. Shi, and W. R. Gao, "Imaginary part-based correlation mapping optical coherence tomography for imaging of blood vessels in vivo," *J. Biomed. Opt.* **20**(11), 116009 (2015).
18. M. Miura, S. Makita, S. Azuma, Y. Yasuno, S. Sugiyama, T. Mino, T. Yamaguchi, T. Agawa, T. Iwasaki, Y. Usui, N. A. Rao, and H. Goto, "Evaluation of retinal pigment epithelium layer change in Vogt-Koyanagi-Harada disease with multicontrast optical coherence tomography," *Invest. Ophthalmol. Visual Sci.* **60**(10), 3352–3362 (2019).
19. E. Borrelli, R. Sacconi, M. Brambati, F. Bandello, and G. Querques, "In vivo rotational three-dimensional OCTA analysis of microaneurysms in the human diabetic retina," *Sci. Rep.* **9**(1), 16789 (2019).
20. O. Jonas, H. Jon, and B. E. J. Gregor, "Advances in optical coherence tomography in dermatology—a review," *J. Biomed. Opt.* **23**(12), 1–10 (2018).
21. J. Lee, W. H. Jang, S. Shim, B. Kim, W.-S. Jang, J. K. Myung, S. Park, and K. H. Kim, "Characterization of early-stage cutaneous radiation injury by using optical coherence tomography angiography," *Biomed. Opt. Express* **11**(5), 2652–2664 (2020).

22. A. J. Deegan, F. Talebi-Liasi, S. Z. Song, Y. D. Li, J. J. Xu, S. J. Men, M. M. Shinohara, M. E. Flowers, S. J. Lee, and R. K. K. Wang, "Optical coherence tomography angiography of normal skin and inflammatory dermatologic conditions," *Lasers Surg. Med.* **50**(3), 183–193 (2018).
23. S. Azuma, S. Makita, D. Kasaragod, S. Sugiyama, M. Miura, and Y. Yasuno, "Clinical multi-functional OCT for retinal imaging," *Biomed. Opt. Express* **10**(11), 5724–5743 (2019).
24. M.-T. Tsai, I. C. Lee, Z.-F. Lee, H.-L. Liu, C.-C. Wang, Y.-C. Choia, H.-Y. Chou, and J.-D. Lee, "In vivo investigation of temporal effects and drug delivery induced by transdermal microneedles with optical coherence tomography," *Biomed. Opt. Express* **7**(5), 1865–1876 (2016).
25. Y. Li, P. Tang, S. Song, A. Rakymzhan, and R. K. Wang, "Electrically tunable lens integrated with optical coherence tomography angiography for cerebral blood flow imaging in deep cortical layers in mice," *Opt. Lett.* **44**(20), 5037–5040 (2019).
26. W. Choi, E. M. Moulton, N. K. Waheed, M. Adhi, B. Lee, C. D. Lu, T. E. de Carlo, V. Jayaraman, P. J. Rosenfeld, J. S. Duker, and J. G. Fujimoto, "Ultrahigh-speed, swept-source optical coherence tomography angiography in nonexudative age-related macular degeneration with geographic atrophy," *Ophthalmology* **122**(12), 2532–2544 (2015).
27. S. B. Ploner, E. M. Moulton, W. Choi, N. K. Waheed, B. Lee, E. A. Novais, E. D. Cole, B. Potsaid, L. Husvogt, J. Schottenhamml, A. Maier, P. J. Rosenfeld, J. S. Duker, J. Hornegger, and J. G. Fujimoto, "Toward quantitative optical coherence tomography angiography: visualizing blood flow speeds in ocular pathology using variable interscan time analysis," *Retina* **36**(Suppl 1), S118–S126 (2016).
28. E. Zudaire, L. Gambardella, C. Kurcz, and S. Vermeren, "A computational tool for quantitative analysis of vascular networks," *PLoS One* **6**(11), e27385 (2011).
29. L. Beckmann, X. Zhang, N. A. Nadkarni, Z. Cai, A. Batra, D. P. Sullivan, W. A. Muller, C. Sun, R. Kuranov, and H. F. Zhang, "Longitudinal deep-brain imaging in mouse using visible-light optical coherence tomography through chronic microprism cranial window," *Biomed. Opt. Express* **10**(10), 5235–5250 (2019).
30. M. Foddis, K. Winek, K. Bentele, S. Mueller, S. Blumenau, N. N. Reichhart, S. Crespo-Garcia, D. Harnett, A. Ivanov, A. Meisel, A. Jousseaume, O. Strauss, D. Beule, U. Dirnagl, and C. Sassi, "An exploratory investigation of brain collateral circulation plasticity after cerebral ischemia in two experimental C57BL/6 mouse models," *J. Cereb. Blood Flow Metab.* **40**(2), 276–287 (2020).
31. J. H. Meyer, P. P. Larsen, C. Strack, W. M. Harmening, T. U. Krohne, F. G. Holz, and S. Schmitz-Valckenberg, "Optical coherence tomography angiography (OCT-A) in an animal model of laser-induced choroidal neovascularization," *Exp. Eye Res.* **184**, 162–171 (2019).
32. L. S. Carroll, H. Uehara, D. Fang, S. Choi, X. Zhang, M. Singh, Z. Sandhu, P. M. Cummins, T. M. Curtis, A. W. Stitt, B. J. Archer, and B. K. Ambati, "Intravitreal AAV2.COMP-Ang1 attenuates deep capillary plexus expansion in the aged diabetic mouse retina," *Invest. Ophthalmol. Visual Sci.* **60**(7), 2494–2502 (2019).
33. Y. Sugano, T. Sekiryu, M. Furuta, R. Tomita, H. Shintake, H. Maehara, and A. Ojima, "Morphometrical evaluation of the choriocapillaris imaged by swept-source optical coherence tomography angiography," *Clin. Ophthalmol.* **12**, 2267–2276 (2018).
34. X. Wei, T. T. Hormel, S. H. Pi, Y. K. Guo, Y. F. Jian, and Y. L. Jia, "High dynamic range optical coherence tomography angiography (HDR-OCTA)," *Biomed. Opt. Express* **10**(7), 3560–3571 (2019).
35. A. Q. Zhang, Q. Q. Zhang, C. L. Chen, and R. K. K. Wang, "Methods and algorithms for optical coherence tomography-based angiography: a review and comparison," *J. Biomed. Opt.* **20**(10), 100901 (2015).
36. R. F. Spaide, J. G. Fujimoto, N. K. Waheed, S. R. Sadda, and G. Staurengi, "Optical coherence tomography angiography," *Prog. Retinal Eye Res.* **64**, 1–55 (2018).
37. M. Arya, R. Rashad, O. Sorour, E. M. Moulton, J. G. Fujimoto, and N. K. Waheed, "Optical coherence tomography angiography (OCTA) flow speed mapping technology for retinal diseases," *Expert Rev. Med. Devices* **15**(12), 875–882 (2018).
38. H. C. Lee, O. O. Ahsen, K. Liang, Z. Wang, C. Cleveland, L. Booth, B. Potsaid, V. Jayaraman, A. E. Cable, H. Mashimo, R. Langer, G. Traverso, and J. G. Fujimoto, "Circumferential optical coherence tomography angiography imaging of the swine esophagus using a micromotor balloon catheter," *Biomed. Opt. Express* **7**(8), 2927–2942 (2016).
39. A. F. Fercher and J. D. Briers, "Flow visualization by means of single-exposure speckle photography," *Opt. Commun.* **37**(5), 326–330 (1981).
40. B. Braaf, K. A. Vermeer, K. V. Vienola, and J. F. de Boer, "Angiography of the retina and the choroid with phase-resolved OCT using interval-optimized backstitched B-scans," *Opt. Express* **20**(18), 20516–20534 (2012).
41. J. V. Migacz, I. Gorczynska, M. Azimipour, R. Jonnal, R. J. Zawadzki, and J. S. Werner, "Megahertz-rate optical coherence tomography improves the contrast of the choriocapillaris and choroid in human retinal imaging," *Biomed. Opt. Express* **10**(1), 50–65 (2019).
42. Y. J. Hong, S. Makita, F. Jaillon, M. J. Ju, E. J. Min, B. H. Lee, M. Itoh, M. Miura, and Y. Yasuno, "High-penetration swept source Doppler optical coherence angiography by fully numerical phase stabilization," *Opt. Express* **20**(3), 2740–2760 (2012).
43. L. I. o. America, "American National Standards for Safe Use of Lasers in Health Care," ANSI Z136.1-2014, 83–87 (2014).